

# Sub-nanotesla Sensitivity at the Nanoscale with a Single Spin

Zhiyuan Zhao,<sup>1,2,\*</sup> Xiangyu Ye,<sup>1,2,\*</sup> Shaoyi Xu,<sup>1,2</sup> Pei Yu,<sup>1,2</sup> Zhiping Yang,<sup>1,2</sup> Xi Kong,<sup>3</sup> Ya Wang,<sup>1,2,4</sup> Tianyu Xie,<sup>1,2,†</sup> Fazhan Shi,<sup>1,2,4,‡</sup> and Jiangfeng Du<sup>1,2,4,§</sup>

<sup>1</sup>*CAS Key Laboratory of Microscale Magnetic Resonance and School of Physical Sciences, University of Science and Technology of China, Hefei 230026, China*

<sup>2</sup>*CAS Center for Excellence in Quantum Information and Quantum Physics, University of Science and Technology of China, Hefei 230026, China*

<sup>3</sup>*National Laboratory of Solid State Microstructures and Department of Physics, Nanjing University, Nanjing 210093, China*

<sup>4</sup>*Hefei National Laboratory, University of Science and Technology of China, Hefei 230088, China*

High-sensitivity detection of microscopic magnetic field is essential in many fields. Here we report that a sensitivity of  $0.6 \text{ nT}/\sqrt{\text{Hz}}$  is achieved experimentally with a 30-nm-deep nitrogen-vacancy defect in diamond. The achieved sensitivity is substantially enhanced by integrating with multiple quantum techniques, including real-time-feedback initialization, dynamical decoupling with shaped pulses, repetitive readout via quantum logic, and so forth. Our results represent the best performance combining magnetic sensitivity and spatial resolution. Therefore, our magnetic sensors will shed new light on searching new physics beyond the standard model, investigating microscopic magnetic phenomena in condensed matters, and detection of life activities at the sub-cellular scale.

Along with the advances in science, more investigations are focusing on the microscopic regime, and naturally require the detection of magnetic field at the microscale [1–11]. For instance, magnetic sensors have been used to search for new interactions beyond the standard model [2, 4]. It is inevitable to build a microscopic sensor with an extremely high sensitivity for exploring interactions in the short-range regime [3, 12]. In condensed matters, observations of some nanoscale magnetic phenomena, like antiferromagnetic domains with extremely weak magnetization [6] and novel behaviors in mesoscopic superconductors [5, 7], also have similar requirements. Biological applications at the microscale, especially for biochemical reactions at the sub-cellular level and nuclear magnetic resonance imaging of a single cell [9], demand both sub-nanotesla sensitivity and sub-micron spatial resolution.

However, the performances of the magnetometers invented so far are still to be improved for the applications above. As the most sensitive magnetic sensor, superconducting quantum interference devices (SQUIDs) can provide sub-femtotesla sensitivity at the macroscale [13], but working at a smaller scale will dramatically worsen its sensitivity, e.g., tens of  $\text{nT}/\sqrt{\text{Hz}}$  at  $\sim 100$  nanometers [14]. On the other hand, single nitrogen-vacancy (NV) centers in diamond have an extraordinary performance at the nanoscale but still with a poor sensitivity of tens of  $\text{nT}/\sqrt{\text{Hz}}$  at best [1]. Other (more than twenty) kinds of magnetometers have similar behaviors, among which the most prominent are optically pumped magnetometers (OPM) [15], Bose-Einstein condensates (BEC) [16], and ensemble NV centers [17]. It seems not realistic to perform a high-spatial-resolution detection without impairing the sensitivity, which may be constrained by the laws of physics. As a potential quantum limit, the energy resolution limit  $E_R = \hbar$  (ERL) is put forward to quantitatively portrait the contradiction. Up to now, all kinds of magnetometers comply with the ERL [18, 19].

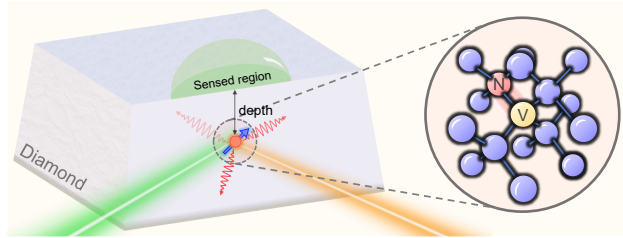


FIG. 1. **Experimental system.** Diagram of a single near-surface NV center in diamond. The depth of the NV center determines the dimension of the sensed region. The 532-nm green laser is used for readout of NV electron spin by collecting fluorescence and mixing charge states, and the 594-nm orange laser is used for readout of charge state in real-time-feedback initialization. Inset: the atomic structure of the NV center in diamond lattice.

In this work, to overcome the aforementioned problem to some extent, we experimentally achieve a sensitivity of  $0.6 \text{ nT}/\sqrt{\text{Hz}}$  with a 30-nm-deep NV center. The NV center is a point defect that consists of a substitutional nitrogen atom and an adjacent vacancy, as shown in Fig. 1, and resides near the diamond surface. The depth is the minimum distance that a sample to be detected can approach, and thus determines the spatial resolution [1, 20]. In our work, the depth of the NV center is measured by detecting the nuclear magnetic resonance from the proton sample put upon the diamond surface [21] (see Supplemental Material for more details). The detected signal mainly originates from the protons at a distance comparable to the NV depth, which justifies taking the depth as the achieved spatial resolution.

By comprehensively considering multiple experimental limitations, including spin decoherence, initialization and readout errors, and duty cycle, the magnetic sensitivity  $\eta_B$  for an individual NV center can be accurately

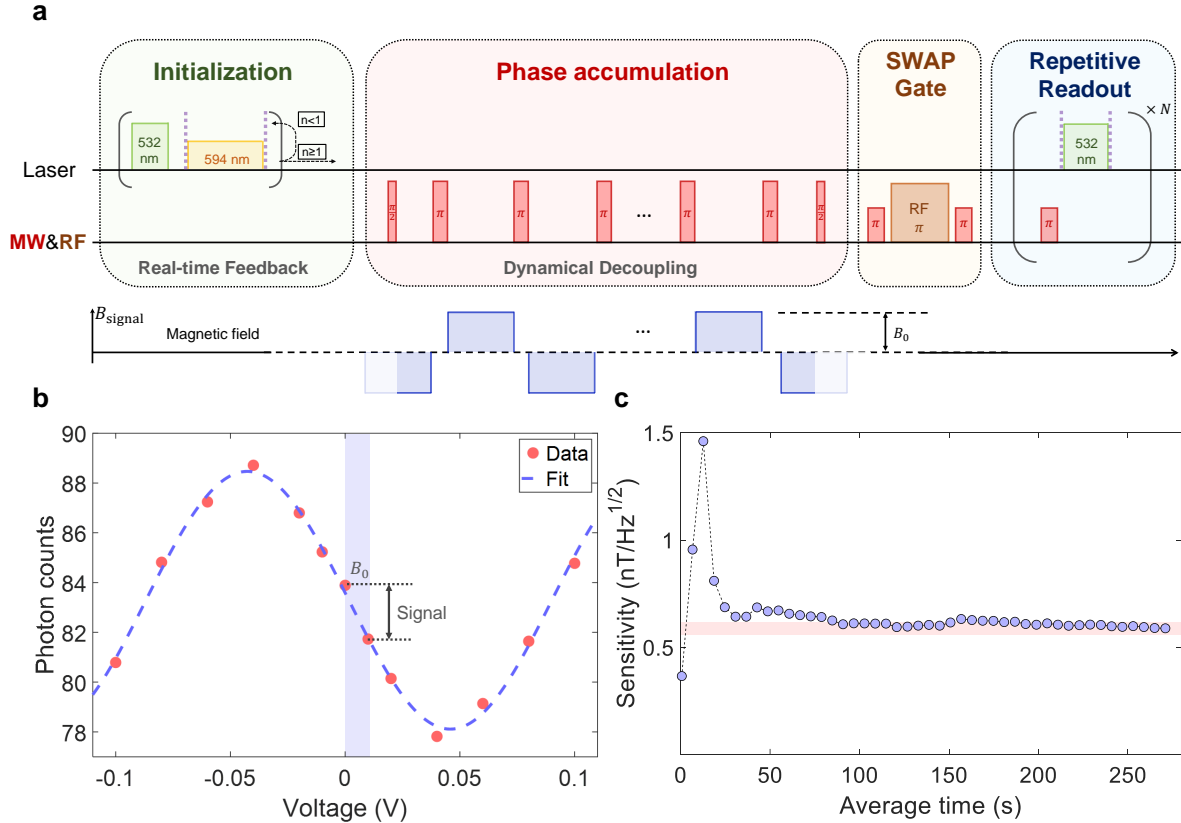


FIG. 2. **Magnetic field measurement.** (a) The experimental sequence comprised of initialization, phase accumulation, and readout. Real-time feedback is performed to initialize the NV charge state. The magnetic field is measured by encoding it into an accumulated phase using dynamical decoupling sequences. The technique of repetitive readout is employed to improve the readout fidelity. Fluorescence photons are collected during the intervals between two purple dashed lines. The waveform  $B_{\text{signal}}$  is generated by the AWG and fed into a coil to produce a small magnetic field. See more details in Fig. S3 of the Supplemental Material. (b) The interference pattern for magnetic sensing as a function of the AWG voltage. The dashed line is given by fitting the experimental data. (c) The magnetic sensitivity measured as a function of the average time in the experiment.

formulated as

$$\eta_B = \frac{1}{\gamma_e \sqrt{T_C}} \cdot \frac{1}{CF_r F_i} \cdot \sqrt{1 + \frac{T_{ir}}{T_C}} \quad (1)$$

where  $\gamma_e$  is the gyromagnetic ratio of the electron spin,  $T_C$  is the time for phase accumulation, and  $C$  is the remained spin coherence at  $T_C$ . The initialization and the readout are both imperfect with  $F_i$  and  $F_r$  denoting their respective fidelities, and occupy considerable time  $T_{ir}$  leading to a reduced duty cycle. For the near-surface NV center that is exposed to the noise of the diamond surface, the coherence time is shortened dramatically down to tens of microseconds [22], compared with several milliseconds for NV centers deep inside a bulk diamond [23]. For the initialization of the NV center by 532-nm laser illumination, there exist two charge states, of which the useful NV<sup>-</sup> state occupies  $\sim 70\%$  and the left is the useless NV<sup>0</sup> state [24]. The percentage of the NV<sup>-</sup> state would be further reduced with shallower NV centers [25]. On the optical readout of the NV spin state, the readout fidelity  $F_r$  is rather low,  $\sim 3\%$  for typical fluorescence

collection efficiencies. Substituting the values above into the Eq. 1 gives the sensitivity roughly  $0.1 \text{ }\mu\text{T}/\sqrt{\text{Hz}}$  for typical 10-nm-deep NV centers.

Improving the NV spin coherence is of paramount importance. Apart from directly enhancing the sensitivity, long coherence times also enable the use of some time-consuming quantum techniques without dramatically decreasing duty cycles. In order to attenuate the adverse effect from the surface noise, we choose to use NV centers with depths of 10-100 nm combined with the technique of dynamical decoupling [26]. Using an XY16-512 sequence, the coherence time is extended from  $146 \pm 5 \text{ }\mu\text{s}$  to  $2.0 \pm 0.2 \text{ ms}$  for the NV center with a depth of  $31.7 \pm 1.1 \text{ nm}$ . Besides, the magnetic noise from  $^{13}\text{C}$  nuclear spins in diamond lattice is removed by  $^{12}\text{C}$  isotope purification.

With millisecond-scale spin coherence, two quantum techniques, real-time feedback for NV negative state preparation [24] and repetitive readout via quantum logic [1], can be integrated into the measurement sequence to improve initialization and readout fidelities. Through hundreds of real-time feedback loops (the first block of

Fig. 2a), the  $\text{NV}^-$  state can be picked out with a 99% success rate [24], but too many loops will degrade the sensitivity. After the sensitivity is optimized, the initialization fidelity of  $\text{NV}^-$  state is better than 92% (see Supplemental Material). High-fidelity readout is realized by transferring the NV spin state to the nuclear spin of the adjacent nitrogen atom through a SWAP gate, then followed by thousands of readouts of the nuclear spin (the last two blocks of Fig. 2a). The nondestructive nature of the nuclear spin after every readout is ensured by a high magnetic field (7662 G in our setup). The number of readout cycles is also optimized for the optimal sensitivity, and executing 2500 cycles (1.44 ms) gives a fidelity of roughly 84%.

The interference sequence for magnetic field measurement is plotted in Fig. 2a, composed of initialization, phase accumulation and readout. The dynamical decoupling sequences in the second block are used to encode the detected magnetic field into the phase of the NV spin. It is worth noting that the use of high-frequency microwaves (MWs) and the existence of the  $^{15}\text{N}$  hyperfine coupling make it rather difficult to apply strong  $\pi/2$  and  $\pi$  pulses for the NV electron spin. Therefore, shaped  $\pi/2$  and  $\pi$  pulses optimized by the gradient ascent pulse engineering (GRAPE) algorithm [27] are adopted here for a lower amplitude and a higher fidelity (see Supplemental Material for more details). The detected magnetic field is produced by a copper coil into which a waveform output from an arbitrary waveform generator (AWG) is fed. Changing the AWG voltage varies the number of collected photons in Fig. 2b. The detected magnetic fields are determined with the coefficient  $\approx 112 \text{ nT/V}$ , which is obtained by fitting the interference pattern. With a specific magnetic field applied, the sensitivity of our system is given by the asymptotic behavior in Fig. 2c, after averaging the data for several hundred seconds (see Supplemental Material).

To find how the sensitivity is affected by the noise from the diamond surface, NV centers with different depths are investigated. By repeating the established procedures

above, the sensitivities for six NV centers are measured and displayed in Fig. 3. The sensitivity is improved gradually as the NV depth increases, and saturates at about  $0.5 \text{ nT}/\sqrt{\text{Hz}}$ . It implies that the effect of the surface noise is no longer the major limiting factor when the depth reaches  $\sim 30 \text{ nm}$ . By the way, the sensitivity of  $0.5 \text{ nT}/\sqrt{\text{Hz}}$  is the highest record for a single NV center at room temperature.

With both high-sensitivity and high-spatial-resolution sensors, we are intended to use the energy resolution limit (ERL) to benchmark them in the following discussions. As detailedly discussed in the literature [19], the ERL quantitatively depicts the contradiction between the spatial resolution and the sensitivity. Among all magnetometers, the optimal energy resolution achieved is close to  $E_R = \hbar$ , but so far none has surpassed it [19] (see Fig. 4a). The ERL combines field, temporal, and spatial resolution in a concise form, which simply reads

$$E_R \equiv \frac{\langle \delta B^2 \rangle T l_{\text{eff}}^3}{2\mu_0} \geq \hbar \quad (2)$$

where  $E_R$  is the energy resolution per bandwidth, and greater than the Planck's constant  $\hbar$ . In the expression of  $E_R$ ,  $\mu_0$  is the vacuum permeability,  $T$  is the measurement time,  $\langle \delta B^2 \rangle$  is the magnetic field variance, and the sensitivity  $\eta_B = \langle \delta B^2 \rangle^{1/2} \sqrt{T}$ . The symbol  $l_{\text{eff}}$  represents the effective linear dimension of the sensor, and determines the spatial resolution.

The ERL is actually not a universally proven quantum limit, though strictly derived for SQUIDs [28] and spin-precession ensembles [29] under some general assumptions. Recently, a theoretical scheme has been proposed to surpass the ERL by using ferromagnetic torque sensors [12]. Additionally, single quantum systems (SQSs), e.g. single NV centers and trapped ions, also have the potential to surpass the ERL [19]. The effective linear dimension  $l_{\text{eff}}$  for SQSs is not the size of the system wavefunction, but the spatial resolution that can be achieved, which manifests the practical significance of the ERL. In this respect, as analogous to ensemble sensors (e.g. OPM, BEC, and NV ensembles), shrinking  $l_{\text{eff}}$  for SQSs always dramatically increases the noise and then shortens coherence times, for which the measurements performed by SQSs are still not below the ERL either [1, 19, 30].

To find the optimal energy resolution in our work, by multiplying the spatial resolutions achieved by detecting external nuclear spins respectively, the energy resolutions for six NV centers are obtained (see Table S2 of the Supplemental Material). The optimal energy resolution given by the 31.7-nm-deep NV center (NV3 in Fig. 3) is  $0.042 \pm 0.001 \hbar$ , well below the ERL by  $13.8 \pm 0.1 \text{ dB}$ . As displayed in Fig. 4a, it gives the best energy resolution among the reported hitherto for all available magnetometers.

Essentially, the ERL constrains the noise level at a certain dimension that the magnetic sensor with that di-

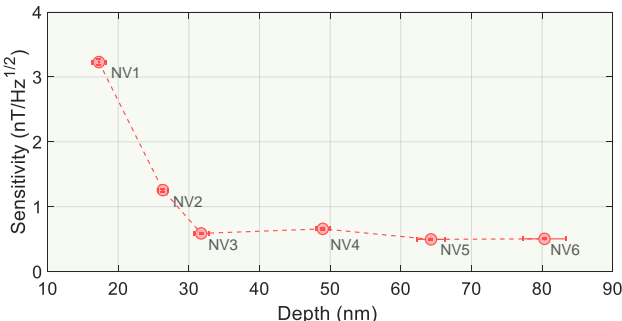
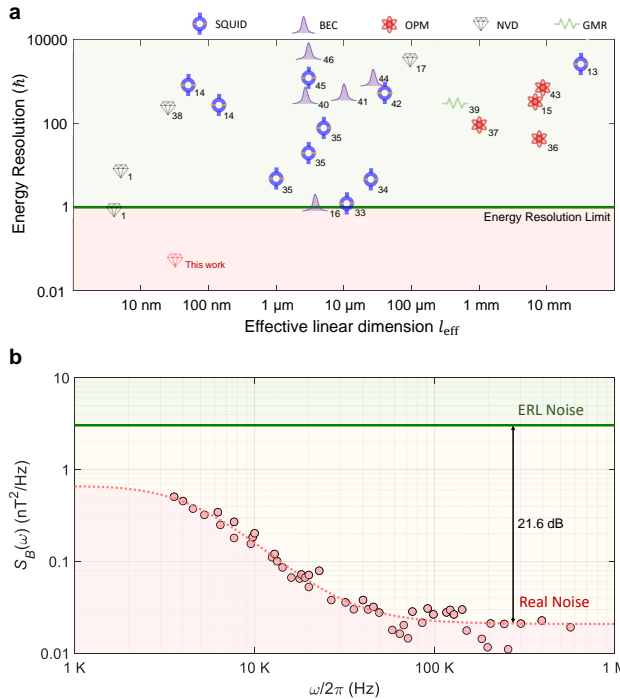


FIG. 3. **Magnetic field sensitivity.** Measured magnetic field sensitivities for six near-surface NV centers with different depths below the diamond surface.



**FIG. 4. Energy resolution per bandwidth and measured noise spectrum.** (a) Reported energy resolution per bandwidth  $E_R$  for different magnetometers versus their effective linear dimensions  $l_{\text{eff}}$ . Line shows  $E_R \equiv \langle \delta B^2 \rangle T_{\text{eff}}^3 / (2\mu_0) = \hbar$ . The energy resolution of NV3 in Fig. 3 is labeled with “This work”. SQUID, superconducting quantum interference device; BEC, Bose-Einstein condensate; OPM, optically pumped magnetometer; NVD, nitrogen-vacancy center in diamond; GMR, giant magnetoresistance. See more details in References with the labeled numbers and in Table S1 of the Supplemental Material. (b) The noise spectral density of the same NV in (a) is measured under multiple dynamical decoupling sequences. The red dashed line is the Lorentzian fitting. The noise level constrained by the ERL is indicated by the green solid line (ERL noise). The noise densities for the frequencies greater than 100 kHz are 21.6 dB below the ERL noise.

dimension must comply with. Therefore, we proceed to investigate whether the noise felt by the NV center is below the ERL or not. The noise spectrum [31] for the NV center with the optimal energy resolution (NV3) is derived from its decoherence behaviors under multiple dynamical decoupling sequences (see Supplemental Material). As shown in Fig. 4b, the measured noise spectral densities are all well below those constrained by the ERL, and 21.6 dB below for the frequencies above 100 kHz. The extent surpassed in the aspect of the sensitivity (13.8 dB in this work) can approach the optimal 21.6 dB if initialization and readout fidelities as well as duty cycles in the experiments are further improved.

In conclusion, the main drawbacks for near-surface NV centers, such as short coherence times, low-fidelity initialization, and low-efficiency readout, are all elegantly over-

come by harnessing multiple quantum techniques. The highest sensitivity ( $0.5 \text{ nT}/\sqrt{\text{Hz}}$ ) at the nanoscale is experimentally achieved, signifying that our sensor takes the combined advantages of magnetic field, temporal, and spatial resolution over all other magnetometers. Therefore, it opens up a new exploration region on searching new short-range interactions, microscopic magnetic phenomena in condensed matters, and detection of life activities at the macro-molecule scale, all urgently demanding both good magnetic sensitivity and high spatial resolution. The best energy resolution  $0.042 \pm 0.001 \hbar$  ( $13.8 \pm 0.1$  dB below the ERL) is given by combining the achieved sensitivity and spatial resolution. In the future, it can be further improved by several orders, through reducing the surface noise with surface treatments [1] and suppressing the spin-lattice relaxation with cryogenic temperatures [32].

## ACKNOWLEDGMENTS

This work was supported by the National Natural Science Foundation of China (Grant No. 81788101, 91636217, T2125011), the National Key R&D Program of China (Grant No. 2018YFA0306600, 2016YFA0502400), Innovation Program for Quantum Science and Technology (Grant No. 2021ZD0303204), the CAS (Grant No. XDC07000000, GJJSTD20200001, QYZDY-SSW-SLH004), the Anhui Initiative in Quantum Information Technologies (Grant No. AHY050000), the Fundamental Research Funds for the Central Universities, and the China Postdoctoral Science Foundation (Grant No. 2021M703110). Besides, the diamond used in this work was partially fabricated at the USTC Center for Micro and Nanoscale Research and Fabrication.

\* These authors contributed equally to this work.

† xie1021@ustc.edu.cn

‡ fzshi@ustc.edu.cn

§ djf@ustc.edu.cn

- [1] I. Lovchinsky, A. O. Sushkov, E. Urbach, N. P. de Leon, S. Choi, K. De Greve, R. Evans, R. Gertner, E. Bersin, C. Müller, L. McGuinness, F. Jelezko, R. L. Walsworth, H. Park, and M. D. Lukin, *Science* **351**, 836 (2016).
- [2] M.S. Safronova, D. Budker, D. DeMille, D. F. J. Kimball, A. Derevianko, and C. W. Clark, *Rev. Mod. Phys.* **90**, 025008 (2018).
- [3] X. Rong, M. Jiao, J. Geng, B. Zhang, T. Xie, F. Shi, C. Duan, Y. Cai, and J. Du, *Phys. Rev. Lett.* **121**, 080402 (2018).
- [4] P. Sikivie, *Rev. Mod. Phys.* **93**, 015004 (2021).
- [5] G. Blatter, M. V. Feigel'man, V. B. Geshkenbein, A. I. Larkin, and V. M. Vinokur, *Rev. Mod. Phys.* **66**, 1125 (1994).
- [6] S.W. Cheong, M. Fiebig, W. Wu, L. Chapon, and V. Kiryukhin, *npj Quantum Mater.* **5**, 3 (2020).

[7] L. F. Chibotaru, A. Ceulemans, V. Bruyndoncx, and V. V. Moshchalkov, *Nature* **408**, 833 (2000).

[8] D. S. Wishart, B. D. Sykes, and F. M. Richards, *J. Mol. Biol.* **222**, 311 (1991).

[9] P. Glover and S. P. Mansfield, *Rep. Prog. Phys.* **65**, 1489 (2002).

[10] K. K. Frederick, V. K. Michaelis, B. Corzilius, T. Ong, A. C. Jacavone, R. G. Griffin, and S. Lindquist, *Cell* **163**, 620 (2015).

[11] M. H. Abobeih, J. Randall, C. E. Bradley, H. P. Bartling, M. A. Bakker, M. J. Degen, M. Markham, D. J. Twitchen, and T. H. Taminiau, *Nature* **576**, 411 (2019).

[12] A. Vinante, C. Timberlake, D. Budker, D. F. J. Kimball, A. O. Sushkov, and H. Ulbricht, *Phys. Rev. Lett.* **127**, 070801 (2021).

[13] M. Schmelz, V. Zakosarenko, A. Chwala, T. Schönau, R. Stoltz, S. Anders, S. Linzen, and H.G. Meyer, *IEEE Trans. Appl. Supercond.* **26**, 1 (2016).

[14] D. Vasyukov, Y. Anahory, L. Embon, D. Halbertal, J. Cappens, L. Neeman, A. Finkler, Y. Segev, Y. Myasoedov, M. L. Rappaport, M. E. Huber, and E. Zeldov, *Nat. Nanotechnol.* **8**, 639 (2013).

[15] I. K. Kominis, T. W. Kornack, J. C. Allred, and M. V. Romalis, *Nature* **422**, 596 (2003).

[16] M. Vengalattore, J. M. Higbie, S. R. Leslie, J. Guzman, L. E. Sadler, and D. M. Stamper-Kurn, *Phys. Rev. Lett.* **98**, 200801 (2007).

[17] T. Wolf, P. Neumann, K. Nakamura, H. Sumiya, T. Ohshima, J. Isoya, and J. Wrachtrup, *Phys. Rev. X* **5**, 041001 (2015).

[18] D. Robbes, *Sens. Actuator A Phys.* **129**, 86 (2006).

[19] M. W. Mitchell and S. P. Alvarez, *Rev. Mod. Phys.* **92**, 021001 (2020).

[20] T. Staudacher, F. Shi, S. Pezzagna, J. Meijer, J. Du, C. A. Meriles, F. Reinhard, and J. Wrachtrup, *Science* **339**, 561 (2013).

[21] L. M. Pham, S. J. DeVience, F. Casola, I. Lovchinsky, A. O. Sushkov, E. Bersin, J. Lee, E. Urbach, P. Cappellaro, H. Park, A. Yacoby, M. Lukin, and R. L. Walsworth, *Phys. Rev. B* **93**, 045425 (2016).

[22] B. K. Ofori-Okai, S. Pezzagna, K. Chang, M. Loretz, R. Schirhagl, Y. Tao, B. A. Moores, K. Groot-Berning, J. Meijer, and C. L. Degen, *Phys. Rev. B* **86**, 081406(R) (2012).

[23] E. D. Herbschleb, H. Kato, Y. Maruyama, T. Danjo, T. Makino, S. Yamasaki, I. Ohki, K. Hayashi, H. Morishita, M. Fujiwara, and N. Mizuochi, *Nat. Commun.* **10**, 3766 (2019).

[24] T. Xie, Z. Zhao, X. Kong, W. Ma, M. Wang, X. Ye, P. Yu, Z. Yang, S. Xu, P. Wang, Y. Wang, F. Shi, and J. Du, *Sci. Adv.* **7**, eabg9204 (2021).

[25] D. Bluvstein, Z. Zhang, and A. C. B. Jayich, *Phys. Rev. Lett.* **122**, 076101 (2019).

[26] J. Du, X. Rong, N. Zhao, Y. Wang, J. Yang, and R. B. Liu, *Nature* **461**, 1265 (2009).

[27] N. Khaneja, T. Reiss, C. Kehlet, T. Schulte-Herbrüggen, and S. J. Glaser, *J. Magn. Reson.* **172**, 296 (2005).

[28] C. D. Tesche and J. Clarke, *J. Low Temp. Phys.* **29**, 301 (1977).

[29] M. W. Mitchell, *New J. Phys.* **22**, 053041 (2020).

[30] K. Fang, V. M. Acosta, C. Santori, Z. Huang, K. M. Itoh, H. Watanabe, S. Shikata, and R. G. Beausoleil, *Phys. Rev. Lett.* **110**, 130802 (2013).

[31] Y. Romach, C. Müller, T. Unden, L. J. Rogers, T. Isoda, K. M. Itoh, M. Markham, A. Stacey, J. Meijer, S. Pezzagna, B. Naydenov, L. P. McGuinness, N. Bar-Gill, and F. Jelezko, *Phys. Rev. Lett.* **114**, 017601 (2015).

[32] A. Jarmola, V. M. Acosta, K. Jensen, S. Chemerisov, and D. Budker, *Phys. Rev. Lett.* **108**, 197601 (2012).

[33] M. W. Cromar and P. Carelli, *Appl. Phys. Lett.* **38**, 723 (1981).

[34] D. D. Awschalom, J. R. Rozen, M. B. Ketchen, W. J. Gallagher, A. W. Kleinsasser, R. L. Sandstrom, and B. Bumble, *Appl. Phys. Lett.* **53**, 2108 (1988).

[35] M. Schmelz, V. Zakosarenko, T. Schönau, S. Anders, S. Linzen, R. Stoltz, and H. Meyer, *Supercond. Sci. Technol.* **30**, 014001 (2017).

[36] H. B. Dang, A. C. Maloof, and M. V. Romalis, *Appl. Phys. Lett.* **97**, 151110 (2010).

[37] W. C. Griffith, S. Knappe, and J. Kitching, *Opt. Express* **18**, 27167 (2010).

[38] P. Maletinsky, S. Hong, M. S. Grinolds, B. Hausmann, M. D. Lukin, R. L. Walsworth, M. Loncar, and A. Yacoby, *Nat. Nanotechnol.* **7**, 320 (2012).

[39] M. Pannetier, C. Fermon, G. Le Goff, J. Simola, and E. Kerr, *Science* **304**, 1648 (2004).

[40] C. F. Ockeloen, R. Schmied, M. F. Riedel, and P. Treutlein, *Phys. Rev. Lett.* **111**, 143001 (2013).

[41] Y. Eto, H. Ikeda, H. Suzuki, S. Hasegawa, Y. Tomiyama, S. Sekine, M. Sadgrove, and T. Hirano, *Phys. Rev. A* **88**, 031602 (2013).

[42] L. E. Fong, J. R. Holzer, K. K. McBride, E. A. Lima, F. Baudenbacher, and M. Radparvar, *Rev. Sci. Instrum.* **76**, 053703 (2005).

[43] D. Sheng, S. Li, N. Dural, and M. V. Romalis, *Phys. Rev. Lett.* **110**, 160802 (2013).

[44] A. A. Wood, L. M. Bennie, A. Duong, M. Jasperse, L. D. Turner, and R. P. Anderson, *Phys. Rev. A* **92**, 053604 (2015).

[45] J. Gallop, P. Josephs-Franks, J. Davis, L. Hao, and J. Macfarlane, *Physica C Supercond.* **368**, 109 (2002).

[46] S. Wildermuth, S. Hofferberth, I. Lesanovsky, E. Haller, L. M. Andersson, S. Groth, I. Bar-Joseph, P. Krüger, and J. Schmiedmayer, *Nature* **435**, 440 (2005).

# Supplemental Material for Sub-nanotesla Sensitivity at the Nanoscale with a Single Spin

## Diamond sample

The targeted NV centers reside in a bulk diamond whose top face is perpendicular to the [100] crystal axis and lateral faces are perpendicular to [110]. The top layer with a thickness of several micrometers is grown with an isotopically purified carbon source (99.999%  $^{12}\text{C}$ ). The NV centers were created by 15 keV and 22.5 keV  $^{15}\text{N}^+$  ion implantation in two different regions and followed by annealing in vacuum for 4 hours at 1000 °C. The luminescence rates of the NV centers are distributed within 150~230 kcounts/s.

## Experimental setup

The diamond is mounted on a typical optically detected magnetic resonance confocal setup, synchronized with a microwave bridge by a multichannel pulse blaster (Spincore, PBESR-PRO-500). The 532-nm green laser and the 594-nm orange laser for driving NV electron dynamics, and sideband fluorescence (650–800 nm) go through the same oil objective (Olympus, UPLSAPO 100XO, NA 1.40). To protect the NV center's negative state and longitudinal relaxation time against laser leakage effects, all laser beams pass twice through acousto-optic modulators (AOM) (Gooch & Housego, power leakage ra-

tio  $\sim 1/1,000$ ) before they enter the objective. The fluorescence photons are collected by avalanche photodiodes (APD) (Perkin Elmer, SPCM-AQRH-14) with a counter card (National Instruments, 6612). The ZI AWG also has a built-in counter to perform real-time feedback for preparing NV negative state. The 18.6 GHz and 24.3 GHz MW pulses for manipulating the NV three sublevels are generated from the microwave bridge, coupled with 0.1-10 MHz radio-frequency (RF) pulses for the nuclear spins via a diplexer, and fed together into the coplanar waveguide microstructure. The external magnetic field ( $\approx 7662$  G) is generated from a permanent magnet and aligned parallel to the NV axis through a three-dimensional positioning system. The positioning system, together with the platform holding the diamond and the objective, is placed inside a thermal insulation copper box. The temperature inside the copper box stabilizes down to a sub-mK level through the feedback of the temperature controller (Stanford, PTC10). The overall setup is plotted in Fig. S1.

### The system Hamiltonian

The NV electron spin ( $S = 1$ ) in the ground state of the  $\text{NV}^-$  triplet and the adjacent  $^{15}\text{N}$  nuclear spin ( $I = 1$ ) comprise our nanoscale system. The Hamiltonian with an external magnetic field  $B_0 \approx 7662$  G applied along the axis of the NV is given by

$$H_0 \approx \overbrace{DS_z^2 + \gamma_e B_0 S_z}^{\text{NV}} + \overbrace{\gamma_{\text{N}} B_0 I_z^{\text{N}} + A_{\parallel} S_z I_z^{\text{N}}}^{^{15}\text{N}} \quad (\text{S1})$$

where  $\gamma_e$  and  $\gamma_N$  are the gyromagnetic ratios of the electron spin and the  $^{15}\text{N}$  nuclear spin respectively.  $S_z$  and  $I_z^N$  are the components of three spin operators along the axis of the NV. The hyperfine interaction  $A_{\parallel}$  is roughly 3.03 MHz.  $D \approx 2870$  MHz is the zero-field splitting of the NV ground state. MW and RF with multiple frequencies are imposed to coherently control the electron spin and the  $^{15}\text{N}$  nuclear spin with the control Hamiltonian

$$H_c(t) = \Omega^{\text{MW}}(t) \cos(\omega^{\text{MW}}t + \phi^{\text{MW}}(t))S_x + \Omega^{\text{RF}}(t) \cos(\omega^{\text{RF}}t + \phi^{\text{RF}}(t))I_x^N \quad (\text{S2})$$

We implemented the quantum circuit (Fig. 2a) by transforming into a suitable interaction picture with some rotation-wave approximations.

### Determination of NV depth

In our work, the depth of the NV center is obtained by detecting the nuclear magnetic resonance signal from the proton sample put upon the diamond surface. Glycerine or immersion oil (IMMOIL-F30CC) of the objective is placed upon the diamond surface and the fluctuating magnetic field from the  $^1\text{H}$  nuclear spins in the samples is measured using a XY16-N dynamical decoupling pulse sequence. The fluctuating magnetic field causes an extra decoherence of the NV spin, which is described by<sup>1</sup>

$$C(\tau) \approx \exp \left[ -\frac{2}{\pi^2} \gamma_e^2 B_{\text{RMS}}^2 K(N\tau) \right] \quad (\text{S3})$$

where  $\gamma_e$  is the electron gyromagnetic ratio and  $B_{\text{RMS}}^2$  is the mean square magnetic field produced by the proton spins.  $K(N\tau)$  depends on the pulse sequence, and the coherence

time  $T_{2n}^*$  and the diffusion coefficient of the proton spins<sup>1</sup>. For a diamond with a [100] top surface,  $B_{\text{RMS}}^2$  for the NV depth  $d_{\text{NV}}$  is

$$B_{\text{RMS}}^2 = \rho \left( \frac{\mu_0 \hbar \gamma_n}{4\pi} \right)^2 \left( \frac{5\pi}{96 d_{\text{NV}}^3} \right) \quad (\text{S4})$$

where  $\gamma_n$  is the gyromagnetic ratio of <sup>1</sup>H spins, and  $\rho$  is the nuclear spin number density ( $\rho = 66 \text{ nm}^{-3}$  for glycerine by calculation, and  $\rho = 69.5 \text{ nm}^{-3}$  for the immersion oil measured by EDUMR20-015V-I NMR system). The NV depths can be extracted by fitting with the equations above. The results are summarized below, and more details can be found in Fig. S2.

Nº	1	2	3	4	5	6
Depth (nm)	$17.3 \pm 1.0$	$26.3 \pm 0.7$	$31.7 \pm 1.1$	$49.0 \pm 1.0$	$64.3 \pm 2.0$	$80.3 \pm 3.0$

### Measurement of magnetic sensitivity

In order to determine the magnetic sensitivity experimentally, we first have to measure the number of collected photons  $N_{\text{ph}}$  against the AWG voltage  $V$  proportional to the amplitude of the small magnetic field produced by the coil. The magnetic field magnitude per unit voltage  $B_V$  is obtained by fitting with

$$N_{\text{ph}}(v) = a \sin(\gamma_e T B_V V + \phi) + c \quad (\text{S5})$$

where  $T$  is the interrogation time,  $\gamma_e$  is the gyromagnetic ratio of the NV spin.  $B_V$ ,  $a$ , and  $c$  are the fitting parameters. Subsequently, we apply a specific magnetic signal and measure

the signal-to-noise ratio (SNR) over a range of experimental times. The sensitivity is then determined by

$$\text{Sensitivity} = \frac{\text{Signal amplitude}}{\text{SNR per } \sqrt{\text{unit time}}} \quad (\text{S6})$$

The optimized parameters for six centers are summarized in Table S2, and the corresponding results are displayed in Fig. 2 and Fig. S4.

### Noise analysis

The analysis of the noise felt by the NV center is based on the technique of spectral decomposition<sup>2</sup>. Generally, the spin coherence decays as a function of time

$$C(t) = \exp(-\Delta\phi^2(t)/2) \quad (\text{S7})$$

due to the interactions with surrounding spins. The phase variance  $\Delta\phi^2(t)$  depends on the noise spectrum  $S(\omega)$  of the environment and the filter function  $F_T(\omega)$  of the dynamical decoupling sequence

$$\Delta\phi^2(t) = \gamma_e^2 \int_0^\infty S(\omega) F_T(\omega) \frac{d\omega}{\pi} \quad (\text{S8})$$

The filter function for high-order dynamical decoupling sequences can be approximated as:

$$F_T(\omega) \approx 2\pi T \cdot \frac{4}{\pi^2} \sum_{k=-\infty}^{\infty} \frac{\delta(\omega - (2k+1)\omega_0)}{(2k+1)^2} \quad (\text{S9})$$

where  $T$  is the total evolution time and  $\omega_0 = \pi N/T$ . Combining Eq. S7, S8 and S9, the noise spectral density at frequency  $\omega_0$  is given by

$$\frac{8}{\pi^2} \sum_{k=0}^{\infty} \frac{S((2k+1)\omega_0)}{(2k+1)^2} = \frac{-2 \ln C(T)}{\gamma_e^2 T} \quad (\text{S10})$$

In order to acquire a wide-range noise spectrum, multiple dynamical decoupling sequences with different orders are executed, as shown in Fig. S7. The effect of spin-lattice relaxation is deducted from the decay curve for millisecond-scale spin coherence. Besides, according to Eq. S10, we build an iterative formula for a more accurate calculation

$$S_n(\omega_0) = \frac{\pi^2}{8} S_0(\omega_0) - \sum_{k=1}^{\infty} \frac{S_{n-1}((2k+1)\omega_0)}{(2k+1)^2} \quad (\text{S11})$$

with  $S_0(\omega_0)$  the right side of Eq. S10. When the iteration number  $n$  is large enough,  $S_n(\omega_0)$  converges to the noise spectrum  $S(\omega_0)$ , and generally,  $n=1$  or  $2$  ( $n=1$  in our case) is enough due to its intrinsic fast convergence. Besides, the noise level constrained by the ERL in Fig. 4 is given by

$$S(\omega) = \frac{2\mu_0\hbar}{e \cdot l_{\text{eff}}^3}, \quad (\text{S12})$$

where the number  $e$  in the denominator is originated from the spin decoherence during phase accumulation.

### Real-time feedback for NV<sup>−</sup> preparation

Since the zero-phonon line for NV<sup>−</sup> is 637 nm and for NV<sup>0</sup> is 575 nm, the 594-nm orange laser can excite the NV<sup>−</sup> but can not excite NV<sup>0</sup>. Therefore, the negative charge state

is prepared if one photon is collected during laser illumination<sup>3</sup>. If not, repeat it until one photon is collected. Before photon counting during each cycle, the green laser is switched on to mix charge states. For evading the reduction of duty cycle, the experimental parameters are carefully optimized: 970 ns for state readout, 95 ns for state mixing, and 100 cycles for the upper bound of feedback loops. The results are shown in Fig. [S6](#).

### Optimal control

The high magnetic field ( $\approx 7662$  G) poses challenges to the coherent manipulation of the NV spin in the experiment. The existence of the  $^{15}\text{N}$  hyperfine coupling demands rather strong MW pulses for simultaneous manipulation of the NV spin in two subspaces of the  $^{15}\text{N}$  spin states. However, the use of high-frequency MWs in high magnetic field, due to the great attenuation loss in the circuits, makes it difficult to achieve such strong MW pulses. To achieve high-fidelity manipulation with fairly weak MW pulses, the technique of optimal control is employed in dynamical decoupling sequences, and the shaped pulses are optimized numerically by the GRAPE (gradient ascent pulse engineering) algorithm detailed in Fig. [S5](#).

### Supplementary Reference

1. L. M. Pham, S. J. DeVience, F. Casola, I. Lovchinsky, A. O. Sushkov, E. Bersin, J. Lee, E. Urbach, P. Cappellaro, H. Park, A. Yacoby, M. Lukin, and R. L. Walsworth,

Phys. Rev. B **93**, 045425 (2016). [3](#), [4](#)

2. Y. Romach, C. Müller, T. Unden, L. J. Rogers, T. Isoda, K. M. Itoh, M. Markham, A. Stacey, J. Meijer, S. Pezzagna, B. Naydenov, L. P. McGuinness, N. Bar-Gill, and F. Jelezko, Phys. Rev. Lett. **114**, 017601 (2015). [5](#)

3. T. Xie, Z. Zhao, X. Kong, W. Ma, M. Wang, X. Ye, P. Yu, Z. Yang, S. Xu, P. Wang, Y. Wang, F. Shi, and J. Du, Sci. Adv. **7**, eabg9204 (2021). [7](#)

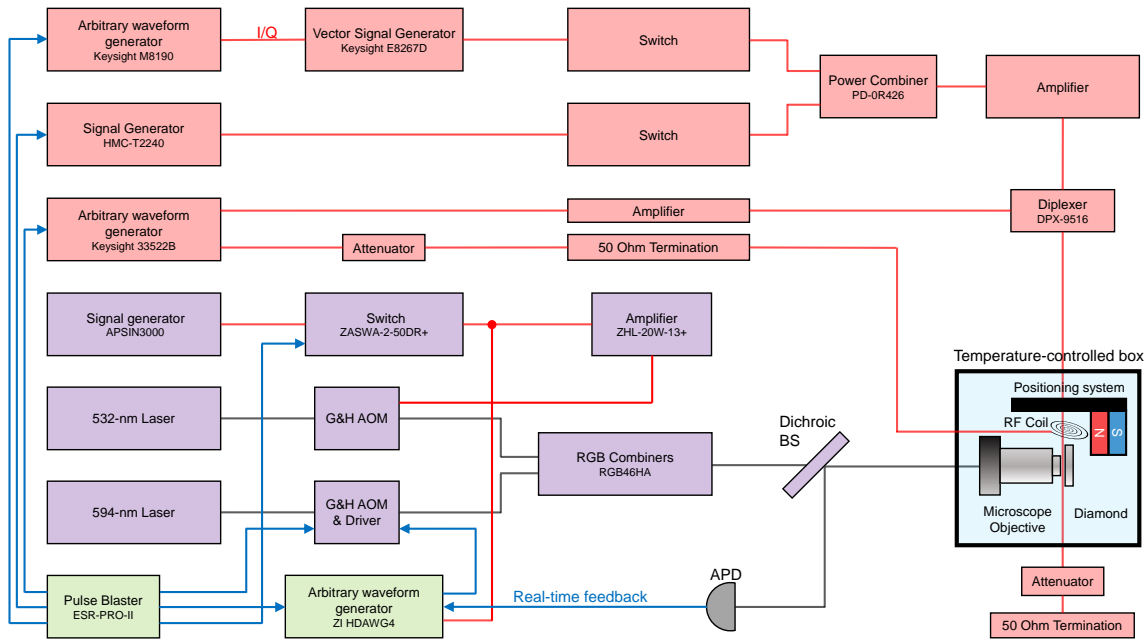
4. M. W. Mitchell and S. P. Alvarez, Rev. Mod. Phys. **92**, 021001 (2020). [9](#)

Table S1. A summary of energy resolution per bandwidth for different magnetometers.<sup>4</sup>

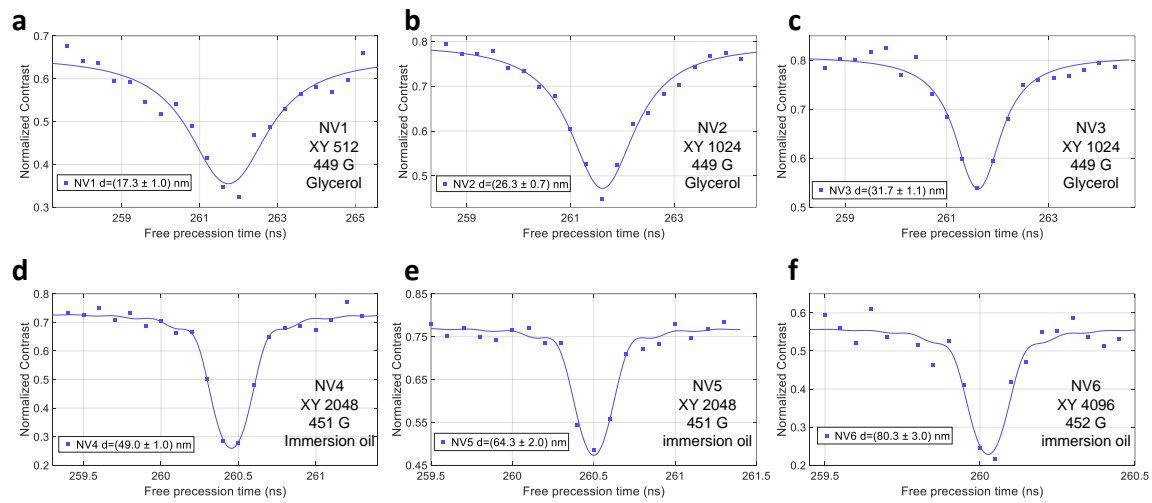
Nº	Type	$l_{\text{eff}}$ (m)	$\eta_B$ (nT/ $\sqrt{\text{Hz}}$ )	Ref.	$E_R(\hbar)$
1	NV	$4.0 \times 10^{-9}$	$5.3 \times 10^{-8}$	1	0.68
2	BEC	$1.1 \times 10^{-5}$	$5.0 \times 10^{-13}$	17	1.24
3	SQUID	$3.7 \times 10^{-6}$	$2.6 \times 10^{-12}$	33	1.34
4	SQUID	$2.5 \times 10^{-5}$	$2.8 \times 10^{-13}$	34	4.68
5	SQUID	$1.0 \times 10^{-6}$	$3.6 \times 10^{-11}$	35	4.89
6	NV	$5.0 \times 10^{-9}$	$1.1 \times 10^{-7}$	1	5.71
7	SQUID	$3.0 \times 10^{-6}$	$1.4 \times 10^{-11}$	35	20.0
8	OPM	$7.6 \times 10^{-3}$	$1.6 \times 10^{-16}$	36	43.5
9	SQUID	$5.0 \times 10^{-6}$	$1.3 \times 10^{-11}$	35	79.7
10	OPM	$1.0 \times 10^{-3}$	$5.0 \times 10^{-15}$	37	94.3
11	NV	$2.5 \times 10^{-8}$	$5.6 \times 10^{-8}$	38	185
12	SQUID	$1.4 \times 10^{-7}$	$5.1 \times 10^{-9}$	13	278
13	GMR	$4.3 \times 10^{-4}$	$3.2 \times 10^{-14}$	39	320
14	OPM	$6.6 \times 10^{-3}$	$5.4 \times 10^{-16}$	16	330
15	BEC	$2.7 \times 10^{-6}$	$7.7 \times 10^{-11}$	40	447
16	BEC	$1.0 \times 10^{-5}$	$1.2 \times 10^{-11}$	41	543
17	SQUID	$4.0 \times 10^{-5}$	$1.5 \times 10^{-12}$	42	543
18	OPM	$8.7 \times 10^{-3}$	$5.4 \times 10^{-16}$	43	726
19	SQUID	$5.0 \times 10^{-8}$	$4.2 \times 10^{-8}$	13	832
20	BEC	$2.7 \times 10^{-5}$	$3.9 \times 10^{-12}$	44	1,148
21	SQUID	$3.0 \times 10^{-6}$	$1.1 \times 10^{-10}$	45	1,233
22	NV	$9.4 \times 10^{-5}$	$9.0 \times 10^{-13}$	18	2,598
23	SQUID	$3.1 \times 10^{-2}$	$1.5 \times 10^{-16}$	12	2,644
24	BEC	$3.0 \times 10^{-6}$	$2.3 \times 10^{-10}$	46	5,389

Table S2. **Experimental parameters and results of our system.** “Total time” means the total time of a single experiment, including initialiation time, interrogation time, and readout time.

Nº	Sequence	Interrogation time	Readout cycles	Total time	Depth (nm)	$\eta_B$ (nT/ $\sqrt{\text{Hz}}$ )	$E_R(\hbar)$
1	XY16-128	0.15 ms	904	0.928 ms	$17.3 \pm 1.0$	$3.23 \pm 0.05$	0.2
2	XY16-512	0.70 ms	1422	1.889 ms	$26.3 \pm 0.7$	$1.26 \pm 0.02$	0.11
3	XY16-512	1.80 ms	2025	3.336 ms	$31.7 \pm 1.1$	$0.59 \pm 0.01$	0.042
4	XY16-512	1.80 ms	1870	3.247 ms	$49.0 \pm 1.0$	$0.66 \pm 0.02$	0.19
5	XY16-512	2.20 ms	2030	3.586 ms	$64.3 \pm 2.0$	$0.50 \pm 0.01$	0.25
6	XY8-32	1.50 ms	1560	2.623 ms	$80.3 \pm 3.0$	$0.51 \pm 0.01$	0.5



**Figure S1: Simplified experimental setup.** The setup mainly consists of microwave (MW) and radio-frequency (RF) circuits (red), optical systems (purple), synchronization and real-time feedback system (green), and a diamond platform inside a temperature-controlled box (blue).



**Figure S2: NMR proton spectra detected by NV centers.** The NV number, the pulse sequence, the applied static magnetic field and the sample are given in the figures. The extracted NV depths are given in the symbol key.

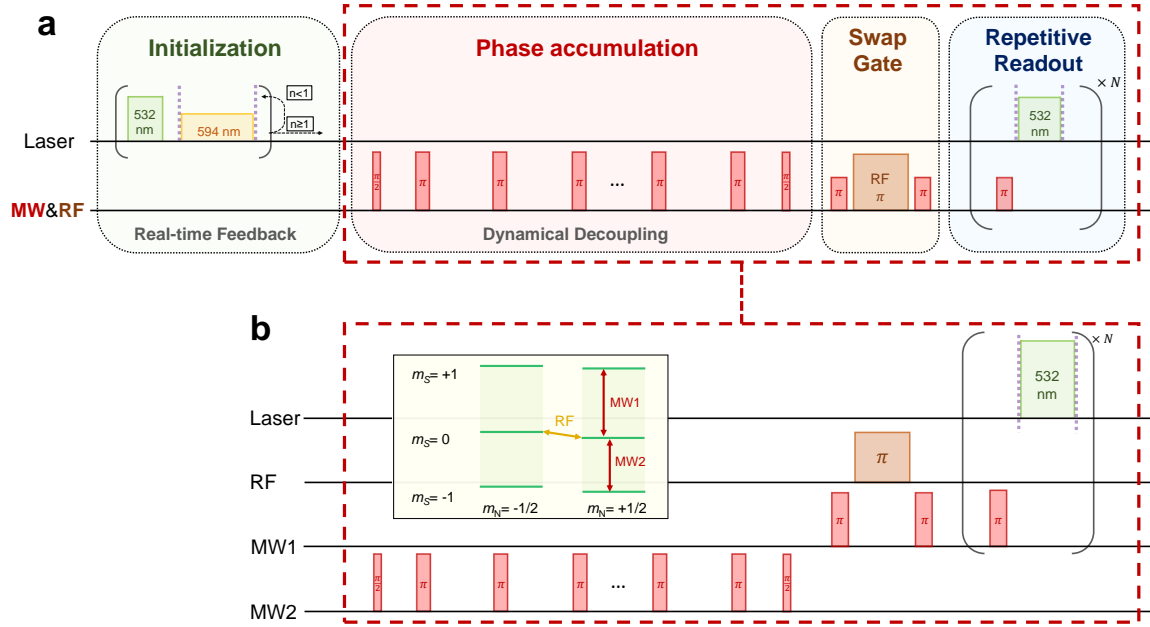


**Figure S3: Details of the interference sequence.** (a) The interference sequence for magnetic field measurement (Fig. 2a in the main text). (b) The details of RF and MW control for the sequence in (a) and the corresponding energy levels of our NV-<sup>15</sup>N system for illustration. The frequencies of RF, MW1 and MW2 are 3.305 MHz, 18.6 GHz and 24.3 GHz, respectively.

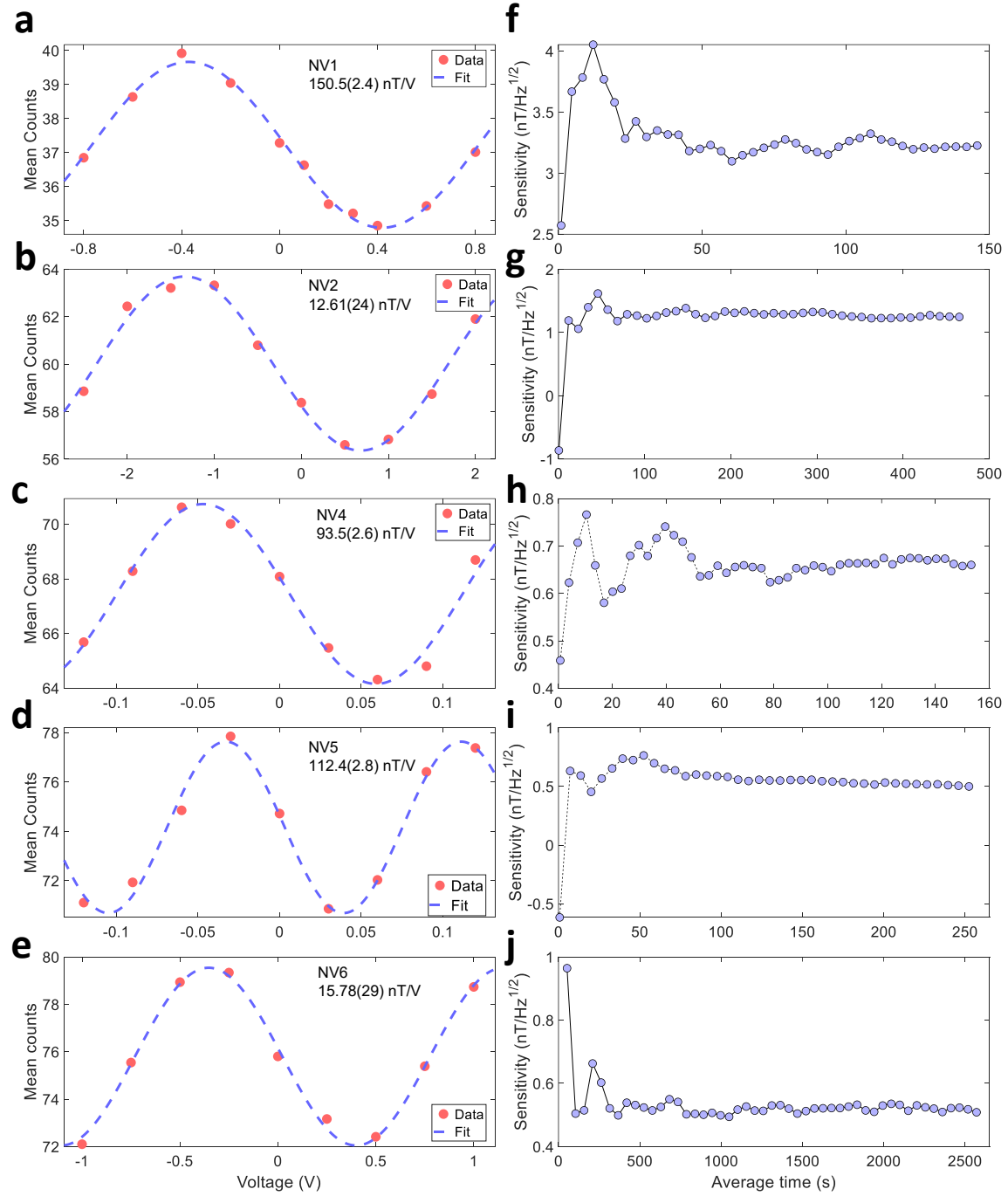


**Figure S4: Magnetic field measurement.** (a)-(e) The interference patterns for magnetic sensing. The dashed lines are given by fitting the experimental data. (f)-(j) The magnetic sensitivities for five NV centers measured as a function of the average times.

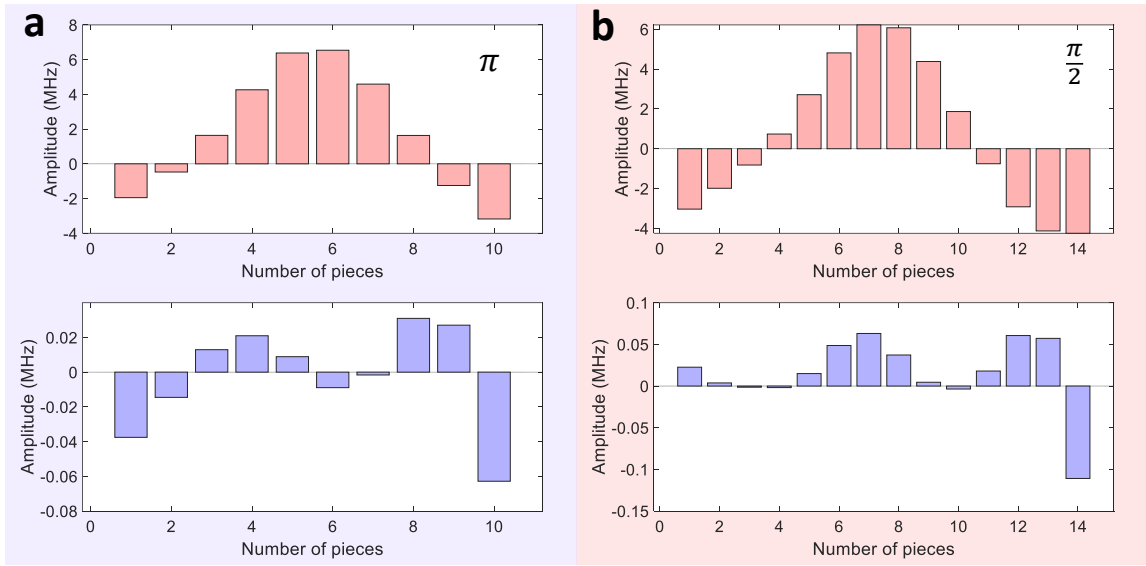


**Figure S5: Optimal control.** (a) The pulse sequence of the real (upper) and imaginary (lower) parts of the  $\pi$  pulses used in dynamical decoupling sequences. The amplitude for each piece is denoted by Rabi frequency. Each piece lasts for 25 ns with 10 pieces in total.

(b) The pulse sequence of the real (upper) and imaginary (lower) parts of the  $\pi/2$  pulses. Each piece lasts for 25 ns with 14 pieces in total.

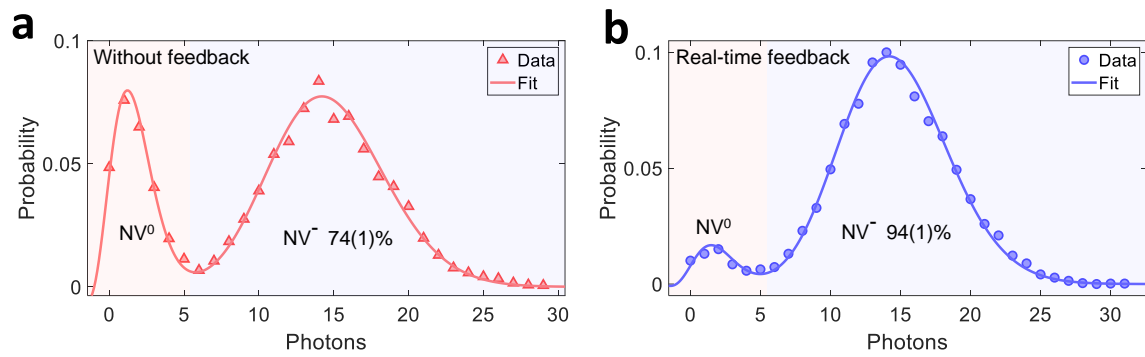


**Figure S6: Real-time feedback for NV<sup>-</sup> preparation.** (a) The distribution of two NV charge states (NV<sup>-</sup> and NV<sup>0</sup>) after initialization without real-time feedback (red triangles, 74% NV<sup>-</sup>). The solid lines are two-peak Poissonian fitting curves for the data points. (b) The distribution of two NV charge states after real-time-feedback initialization (blue circles, 94% NV<sup>-</sup>).

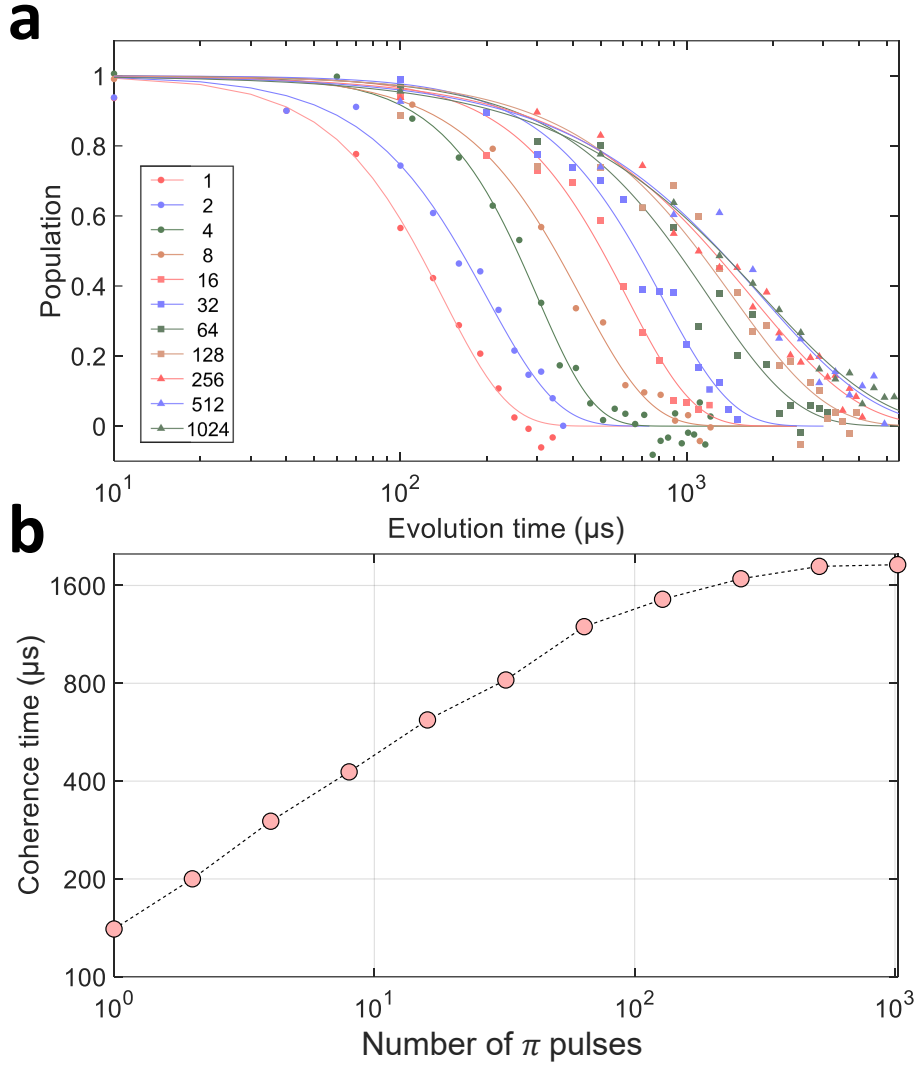


**Figure S7: Decoherence behaviors.** (a) Decoherence behaviors for the NV center with the optimal energy resolution under multiple dynamical decoupling sequences with different numbers of  $\pi$  pulses. The solid lines are the fittings with stretched exponential functions. (b) Coherence times as a function of the number of  $\pi$  pulses of dynamical decoupling sequences.